Room temperature polariton spin switches based on Van der Waals superlattices

Jiaxin Zhao[1,8], Antonio Fieramosca [2,8] ✉, Ruiqi Bao [1,8], Kevin Dini[1], Rui Su [1,3], Daniele Sanvitto[2], Qihua Xiong [4,5,6,7] ✉ & Timothy C. H. Liew[1] ✉

Transition-metal dichalcogenide monolayers possess large exciton binding energy and a robust valley degree of freedom, making them a viable platform for the development of spintronic devices capable of operating at room temperature. The development of such monolayer TMD-based spintronic devices requires strong spin-dependent interactions and effective spin transport. This can be achieved by employing exciton-polaritons. These hybrid light-matter states arising from the strong coupling of excitons and photons allow high-speed in-plane propagation and strong nonlinear interactions. Here, we demonstrate the operation of all-optical polariton spin switches by incorporating a WS_2 superlattice into a planar microcavity. We demonstrate spin-anisotropic polariton nonlinear interactions in a WS_2 superlattice at room temperature. As a proof-of-concept, we utilize these spin-dependent interactions to implement different spin switch geometries at ambient conditions, which show intrinsic sub-picosecond switching time and small footprint. Our findings offer new perspectives on manipulations of the polarization state in polaritonic systems and highlight the potential of atomically thin semiconductors for the development of next generation information processing devices.

Carrying information in both the charge and spin of electrons allows for the realization of complex devices with a high degree of functionality. Starting from the observation of spin-dependent electron transport phenomena and the discovery of giant magnetoresistance in solid-state devices[1], spin-based electronics (spintronics) has become a major research area in condensed-matter physics and information technology, leading to the realization of devices with reduced dimensionality that are now ubiquitous in modern life[2]. Spintronics holds significant potential for the development of next generation ultrafast and cost effective technologies[3,4]. The majority of spintronic applications necessitate robust spin-dependent interactions within

devices, long-distance transfer of spin information, high switching efficacy, high processing speed and integrability.

To properly fulfill these requirements, the concept of spintronics with electrons has been extended to different research areas, spanning from optics[5] to optoelectronics with bounded electron-hole pairs, *i.e.*, excitons[6]. All-optical schemes present long-distance transport and high switching rates but weak nonlinearity. On the other hand, exciton-based optoelectronic devices have good integrability and switching efficacy but limited spin transport, hindered by the low exciton diffusion. In this respect, exciton-polaritons, *i.e.*, hybrid light-matter excitations arising from the strong coupling of excitons and photons,

[1]Division of Physics and Applied Physics, School of Physical and Mathematical Sciences, Nanyang Technological University, Singapore, Singapore. [2]CNR NANOTEC Institute of Nanotechnology, via Monteroni, Lecce, Italy. [3]School of Electrical and Electronic Engineering, Nanyang Technological University, Singapore, Singapore. [4]State Key Laboratory of Low-Dimensional Quantum Physics and Department of Physics, Tsinghua University, Beijing, P.R. China. [5]Frontier Science Center for Quantum Information, Beijing, P.R. China. [6]Beijing Academy of Quantum Information Sciences, Beijing, P.R. China. [7]Beijing Innovation Center for Future Chips, Tsinghua University, Beijing, P.R. China. [8]These authors contributed equally: Jiaxin Zhao, Antonio Fieramosca, Ruiqi Bao. ✉e-mail: antonio.fieramosca@gmail.com; Qihua_xiong@tsinghua.edu.cn; tchliew@gmail.com

have emerged as a promising platform for spintronic devices[7,8]. Owing to their hybrid nature, polaritons exhibit small effective mass and pronounced nonlinearities, leading to long in-plane propagation with high velocities as well as to high switching efficacy processing speed[9–14]. They are spin degenerate and the interaction strength between parallel and antiparallel spin states is different in GaAs-based microcavities[15]. This spin anisotropic interaction has enabled the realization of proof-of-concept polarization-sensitive devices[7,8,16,17], as well as the demonstration of spin multistability[18], which typically rely on a near negligible interaction between antiparallel spins compared to parallel spins. However, the practical implementation of cost-effective and technologically relevant polariton-based spintronic devices requires room temperature operation, which poses a significant challenge for traditional inorganic semiconductors due to their small exciton binding energy[19]. Moreover, efficient devices demand both miniaturization and fast operational time and most of proof-of-concept GaAs-based spintronic devices have large footprint and slow operation time[7,11].

In this respect, transition metal dichalcogenides (TMDs), characterized by large binding energy and strong oscillator strength, have been proposed as a good platform to investigate many body physics and realize technological applications at room temperature. The weak van der Waals interlayer interactions in TMDs allow the exfoliation down to the monolayer (ML) level and the fabrication of complex heterostructures, as well as the integration with optical microcavities, facilitating the design and manufacture of various on-chip photonic and polaritonic devices, such as laser and light emitting diodes[20]. Furthermore, the broken inversion symmetry and strong spin-orbit interaction in TMDs result in pronounced optical selection rules at two energy-degenerate valleys[21]. When TMDs are strongly coupled with microcavities, the valley properties are preserved even at room temperature[22–24]. Demonstrations of the optical valley Hall effect[25], valley selective optical Stark effect[26], optical parametric scattering[27], and valley manipulation under magnetic field[28], further emphasize the significance of TMD polaritons for the development of realistic devices.

Prior studies have been focused mainly on the creation of valley polaritons using non-resonant photoluminescence and largely overlooked the polarization-dependent nonlinear optical properties in TMD polaritons, which are fundamental for the development of innovative polariton-based devices, such as optical spin switches, transistors, and logic gates. Moreover, in comparison to MLs, superlattices of TMDs, where multiple MLs are stacked together with a dielectric spacer in between, exhibit larger optical density and higher absorbance, therefore leading to larger Rabi splitting. This makes them

a unique platform for the control and manipulation of optical properties in TMD-based devices[29–32].

Here, we investigated the spin-dependent interactions in WS_2 superlattice microcavities at room temperature, revealing a robust full spin anisotropy. The presence of spin-dependent polariton interactions is exploited to realize all-optical spin switches. We demonstrate that the ON/OFF polarization switching can be realized within 1 picosecond, in an area of around 25 μm^2. Our results indicate that TMD superlattices are extremely suitable for the implementation of novel designs fully exploiting the spin anisotropy of excitonic-polaritons for the realization of ultrafast and small footprint spintronic devices.

Results

We investigated WS_2 superlattices embedded in a planar dielectric microcavity, as schematically shown in Fig. 1a. The microcavity consists of two distributed Bragg reflectors (DBRs) made of seven pairs of SiO_2/TiO_2 layers each (see "Methods"). The bottom mirror was grown on a glass substrate for the purpose of transmission measurements. The superlattice N3 is composed of alternating layers of WS_2 ML and insulating spacers of SiO_2 with thickness around 4 nm and deposited by E-beam evaporation (see "Methods" for details), as schematically shown in Fig. 1a. Optical microscope images of the sample on the bottom DBR are shown in Supplementary Fig. S1. In the superlattice areas, electronic interaction between each ML is absent when neighboring WS_2 MLs are separated by a SiO_2 layer, thick enough to avoid tunneling. Thus, the superlattice areas preserve the ML optical and electronic properties, while having a higher oscillator strength[30].

To establish the existence of a strong coupling between cavity photons and material excitons, we performed angle-resolved white light reflectance measurements. The microcavity dispersion shows a clear anti-crossing behavior at the exciton resonances and the formation of two new branches, i.e., the lower and upper polariton branches (LPB and UPB), as shown in Fig. 1b for N3 superlattice. The experimental dispersion was accurately described by a two-coupled oscillator model, with a Rabi splitting of around 66 meV, as indicated by the dashed yellow curves in Fig. 1b. The reflectance maps for both ML and N2 superlattice region, as well as the Rabi splitting energy as a function of number of stacked layers are shown in Supplementary Fig. S2. These values are comparable to previous works and proportional to the square root of the number of stacked layers[29,31].

Spin-dependent nonlinearities are critical for the development of polariton physics as well as for the realization of polariton-based spintronic devices. To further explore the potential applications of TMD polaritons, we have studied the polarization-dependent
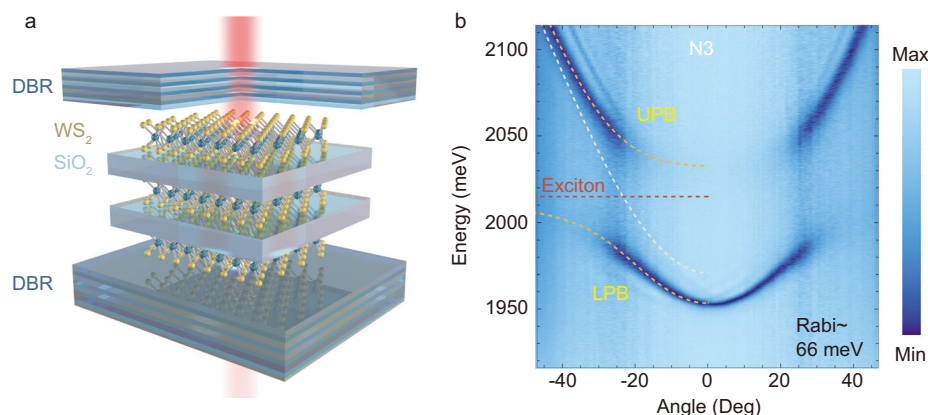
Fig. 1 | Optical characterization of TMDs microcavities. a Schematic of the TMD based microcavities, consisting of WS_2-superlattices sandwiched between two DBRs. **b** The angle-resolved reflectivity map of the superlattice microcavity, collected at room temperature by using a white light source. The two dashed yellow curves are the UPB and LPB dispersions obtained by using a two-coupled oscillator model. The dashed red line and dashed parabola represent the exciton energy and the dispersion of cavity mode, respectively.

interactions under pulsed resonant pumping. Specifically, linear polarization can be considered as a coherent superposition of two counter-polarized circular components. Consequently, under linearly polarized laser excitation, only half of the excited polaritons have the same spin, while under circularly polarized laser excitation, all polaritons are created with the same spin. Therefore, a stronger interaction is expected for the circular polarization while the interaction is halved for the linear polarization, as it has been observed in GaAs-based polaritons[15] and 2D perovskite at room temperature[33–36]. We measured the sample in a transmission configuration by using a femtosecond pulsed laser (100 fs, 1 kHz) that resonantly excites the ground state of the LPB (see "Methods" for details). This allows us to treat the system as a pure polariton system, avoiding the formation of an incoherent and uncoupled exciton reservoir as well as minimizing thermal heat effects.

The normalized transmission spectra for the superlattice microcavity as a function of polariton density with linearly (red curves) and circularly (blue and purple curves) polarized pump are displayed in Fig. 2a. Under both excitation conditions, we observed a continuous blueshift by increasing the polariton density (see "Methods"). The energy shift of the ground state ($\triangle E_{LP}$) for linear (red dots) and circular (light blue dots for $\sigma-$ and dark blue for $\sigma+$) polarized pump is reported in Fig. 2b. The dashed red and blue line represent a linear fit of the experimental data for linear and circular polarization, respectively. As can be immediately seen, the energy shift of the ground state for circularly polarized excitation (blue curves) is higher than that of the linear case (red curves) for the superlattice, therefore confirming a clear modulation in response to changes in the pump polarization state. Moreover, we also checked whether the observed polarization-dependent nonlinearity is affected by a rotation in the linear polarization. Specifically, we measured the blueshift of the ground state as a function of the pumping power for the two orthogonal linear components, TE and TM, respectively. As shown in Supplementary Fig. S3, the blueshift is almost identical for the two linear polarizations.

We then analyze the above reported polarization-resolved nonlinear transmission measurements considering the interaction strengths between polaritons with parallel (α_1), or antiparallel (α_2) spins. The energy shift of the ground state is proportional to α_1 and ($\alpha_1 + \alpha_2$)/2 for circularly and linearly polarized pumps respectively (with the same total intensity). The blueshift ratio measured in different polarizations is then given by ($1+\alpha_2/\alpha_1$)/2 and is equal to the ratio

between the two slopes (L/C) experimentally observed, leading to a $|\alpha_2/\alpha_1|$ ratio of around 0.14 ±0.01 for superlattices. The measured value for the superlattice is consistent with the typical picture of spin-dependent polariton-polariton interactions, where the repulsive interaction is stronger for polaritons with the same spin ($\alpha_1 > 0$) while the interaction for polaritons with different spins is much weaker ($|\alpha_2/\alpha_1| \ll 1$). Moreover, from the above reported data, we also evaluated the exciton-exciton interaction strength for the circular excitation case. The blueshifts of the ground state were well-fitted by a linear function where the slope represents the polariton-polariton interaction constant, according to $\triangle E_{pol} = \alpha_1 n_{pol}$. By considering the excitonic fraction and the following relation $g_{xx} = \alpha_1/|X|^4$ (see Supplementary Fig. S4), we then retrieved an exciton-exciton interaction constant of 0.129 µeVµm². Our present results indicate that our superlattice exhibits a significant spin-anisotropy of polariton interactions, which is a necessary foundation to consider polariton-based spintronic applications.

In traditionally studied GaAs-based systems the dominant mechanism of polariton-polariton interactions comes from the exciton exchange interaction, where pairs of excitons exchange electrons or holes. While this preserves the spin of excitons with the same spin, it results in a conversion of bright excitons to dark excitons when excitons of opposite spin interact, which must be suppressed as dark excitons have a different resonance energy[37]. Consequently, opposite spin excitons tended to rely on a different mechanism of interaction, with scattering through biexcitons understood as a dominant source.

In TMD-based systems, the mechanisms of polariton-polariton interaction are still a topic of debate. While the exchange interaction is still expected, polaron mediated interaction[38,39], trion mediated interaction[40,41], and phase-space filling are discussed[42]. Our present study does not aim to separate these mechanisms, but only point out that a strong spin-anisotropic interaction response is possible with TMD-based microcavities and that a spin-switch can be realized based on it (at room temperature). While the different interaction mechanisms are expected to be weaker in multilayered superlattice samples, as the interacting particles are spread across multiple TMD layers, we believe that phase-space filling can remain significant as the Rabi splitting that it reduces is larger in superlattice samples[31]. We note that phase-space filling should be fully anisotropic, where the filling of an exciton state causes a reduction of the Rabi splitting for the same spin polarization[33].
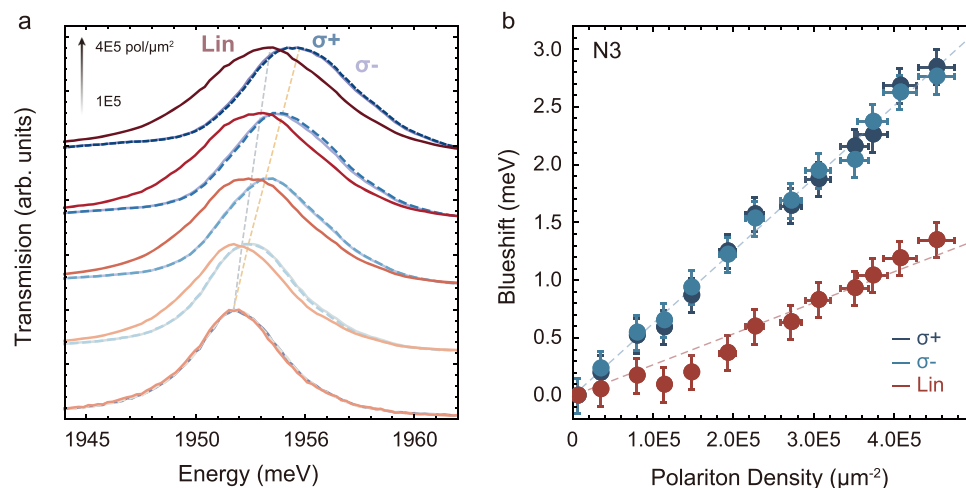
Fig. 2 | Spin-dependent nonlinearities in TMD microcavities. a Resonant transmission spectra of the LPB ground state in superlattice microcavity ($k = 0$) for different excitation powers for linear (red), circular $\sigma+$ (blue) and $\sigma-$ (purple) polarized excitations, respectively. b The blueshift of the ground state as a function of polariton density for linear (red dots) and circular (light blue dots for $\sigma-$ and dark blue for $\sigma+$) polarized excitations for the superlattice microcavity. The dashed red and blue lines are linear fits of the experimental data. The error bars of polariton density in b are explained in the "Methods" section. The error bars on the energy shift data correspond to the 95% confidence interval of a Gaussian fit.

The observation of spin-dependent interactions in superlattice microcavities at room temperature is a crucial advance toward the practical implementation of polariton spintronics. Specifically, by increasing the Rabi splitting of the system, the LPB shifts far in energy from the exciton resonance, therefore limiting the inhomogeneous broadening and keeping a good visibility and suitable excitonic fraction. This is particularly important for the realization of nonlinear polariton devices that usually rely on the resonant excitation of the LPB[8]. It is noteworthy that an increase of the Rabi splitting can also be achieved by decreasing the volume of the optical mode, i.e., by employing different optical platforms such as Bloch surface waves, bound states in the continuum, or plasmons[43–45]. On the other hand, as shown in Supplementary Fig. S2, the ML region of our sample, shows a positive detuning ($\Delta = 0-5$ meV) and the LPB is quite broad, which made it difficult to establish an initially OFF state. Although an increase in the detuning would mitigate the inhomogeneous broadening of the ML sample, the excitonic fraction, and therefore the nonlinear character, would decrease dramatically, making it challenging to observe a significant blueshift. For these reasons, the heterostructure offers the best compromise, naturally mitigating the inhomogeneous broadening and maintaining suitable excitonic fractions far from the exciton resonance.

We take advantage of the spin-dependent interactions and increased Rabi splitting of superlattice polaritons for the realization of polariton spin switches. With the aim of testing the efficiency of our spin switch device, we employed an experimental configuration closely resembling that reported in GaAs-based microcavities. Nevertheless, we conducted our experiments under pulsed excitation conditions, which could be more relevant for switching applications. The microcavity is pumped with two beams: a strong pump beam focused at a given in-plane momentum with energy slightly blue-detuned with respect to the LPB and a weak control beam always resonant with the LPB at $k = 0$, which triggers the transmission of the pump. Both beams were obtained from the same laser pulse that was split into two excitation paths and focused on a spot with a diameter of around 5 μm. Two bandpass filters were used to reduce the laser bandwidth while a motorized stage placed on the control excitation line was employed to synchronize in time the two beams on the sample plane (see "Methods" and Supplementary Fig. S5 for further details). The pump laser is circularly polarized and initially out of resonance (OFF state), therefore with almost zero transmitted intensity, while the control beam is either co- or cross-circular polarized with respect to the pump and always resonant with the ground state of the LPB, as schematically shown in Fig. 3a. The polarization state of both beams has been carefully characterized as shown in Supplementary Fig. S6. The detection line is always co-circular polarized with respect to the pump while the control beam transmitted signal is removed from the detection line by using a filter in momentum space. At low control fluences the system is always in the OFF state for both polarizations while, by increasing the control beam fluence, the presence of polariton-polariton interactions blueshifts the LPB, thus gradually bringing the mode into resonance with the pump beam, therefore resulting in the ON state with high transmitted intensity for the co-circular excitation scheme. This behavior is summarized by the red dotted line in Fig. 3b. The yellow/red region in the left/right part of Fig. 3b indicates the OFF/ON state regions. However, as we discussed above, in systems with spin-dependent interactions, polaritons with parallel spin exhibit stronger interactions than those with antiparallel spin. This peculiarity allows the ON/OFF switch of the pump by either changing the control beam fluence or by simply changing the polarization state of the control from co- to cross-circular polarization, as indicated by the blue dotted line in Fig. 3b. We evaluated the ON-OFF ratio by dividing the transmitted pump intensity in the high-control power regime (ON state, red region) by that in the low-control power regime (OFF state, yellow region), obtaining an on-off ratio of ~100. It is

important to note that this ratio is influenced by critical experimental parameters, including the linewidth of the pump beam, the quality of the microcavity, and the visibility of the LPB, which varies with the wavevector k. The real space images of the transmitted pump in the ON state region for the four different combinations, i.e., pump σ+/control σ+, pump σ+/control σ-, pump σ-/ control σ+, and pump σ-/ control σ- are shown in Fig. 3c–f, respectively. A significant increase in the population of the transmitted pump is only visible when the control beam is co-circularly polarized with the pump (Fig. 3c, f and Supplementary Fig. S7a) while only a weak residual transmission is visible in the cross-polarization schemes (Figs. 3d, e and S7b). This residual emission may be attributed to local imperfections of the sample. The high nonlinearities of TMD microcavities allow the realization of the spin switch at low pumping fluences. The above reported data has been also obtained with a slightly different injection k for the pump, as shown in Supplementary Fig. S8. The above presented data immediately suggest how the device requires a small footprint, comparable to that used in GaAs-based samples, and low pumping power. Indeed, with a pumping power of the probe exceeding 100 nW, the system reaches the ON state.

We investigated the sensitivity of the spin switch to the polarization of the control beam and time delay between the two beams with a fixed pump fluence while keeping the control beam fluence in the ON region depicted in Fig. 3b. The transmitted pump emission integrated in real space is plotted as a function of the ellipticity of the control, which is defined by the parameter θ, where $\theta = 0$ ($\pi/2$) corresponds to σ+ (σ−) circular polarization, as shown in Fig. 3g. When the two beams are co-circularly polarized ($\theta = 0$), a strong signal is observed, indicating that the weak control is sufficient to switch the system from OFF to ON regime. By further increasing θ, the transmitted pump gradually decreases and reaches its minimum at 0.5 rad where the control beam is cross-circularly polarized with respect to the pump. A detailed analysis of the detected polarization state is presented in Supplementary Fig. S9. Here, the transmitted pump intensity for a co-σ+ excitation scheme is plotted as a function of the ellipticity of the detection line, thus confirming that the σ- state is almost empty. In addition, we also monitored the temporal response of the spin switch by scanning the time delay between the two beams kept in the co-σ+ excitation scheme, as shown in Fig. 3h. The transmitted pump reaches its maximum and completely vanishes within 1 ps (at 0.5 ps the transmitted pump signal is decreased by 80%), thus confirming the ultrafast nature of the spin switch. It is important to note that the intrinsic short lifetime of our sample allows an ultrafast switching time that is two orders of magnitude faster than GaAs-based microcavities[11]. Although some proof-of-concept polariton transistors and switches have been proposed by using perovskites and organics[12,13], none of these designs exploited the polarization degree of freedom. This additional degree of freedom, along with the high stability of TMDs, will certainly push them as a leading material platform for room-temperature polaritonic applications, surpassing other active materials that often exhibit significant instability under optical pumping conditions.

An alternative scenario to the circular excitation schemes discussed is for the pump beam to be linearly polarized (superposition of a clockwise and anticlockwise circular polarization), while the control beam is either σ+ or σ-, as schematically shown in Fig. 4a and b, respectively. Even in this case, at high control fluences the system is switched from the OFF to ON state. However, when the system reaches the ON state, a rotation of the control beam polarization state from clockwise to anticlockwise leads to a similar rotation of the transmitted pump polarization. To underline this effect, we detected the real space images of the transmitted pump kept in the linear polarization (vertical) by changing either the polarization state of the control or of the detection line, which are presented in Fig. 4c−f for control σ+/det σ+, control σ+/det σ-, control σ-/det σ+ and control σ-/det σ-, respectively. We performed theoretical simulations (Fig. 4g−j) by solving the
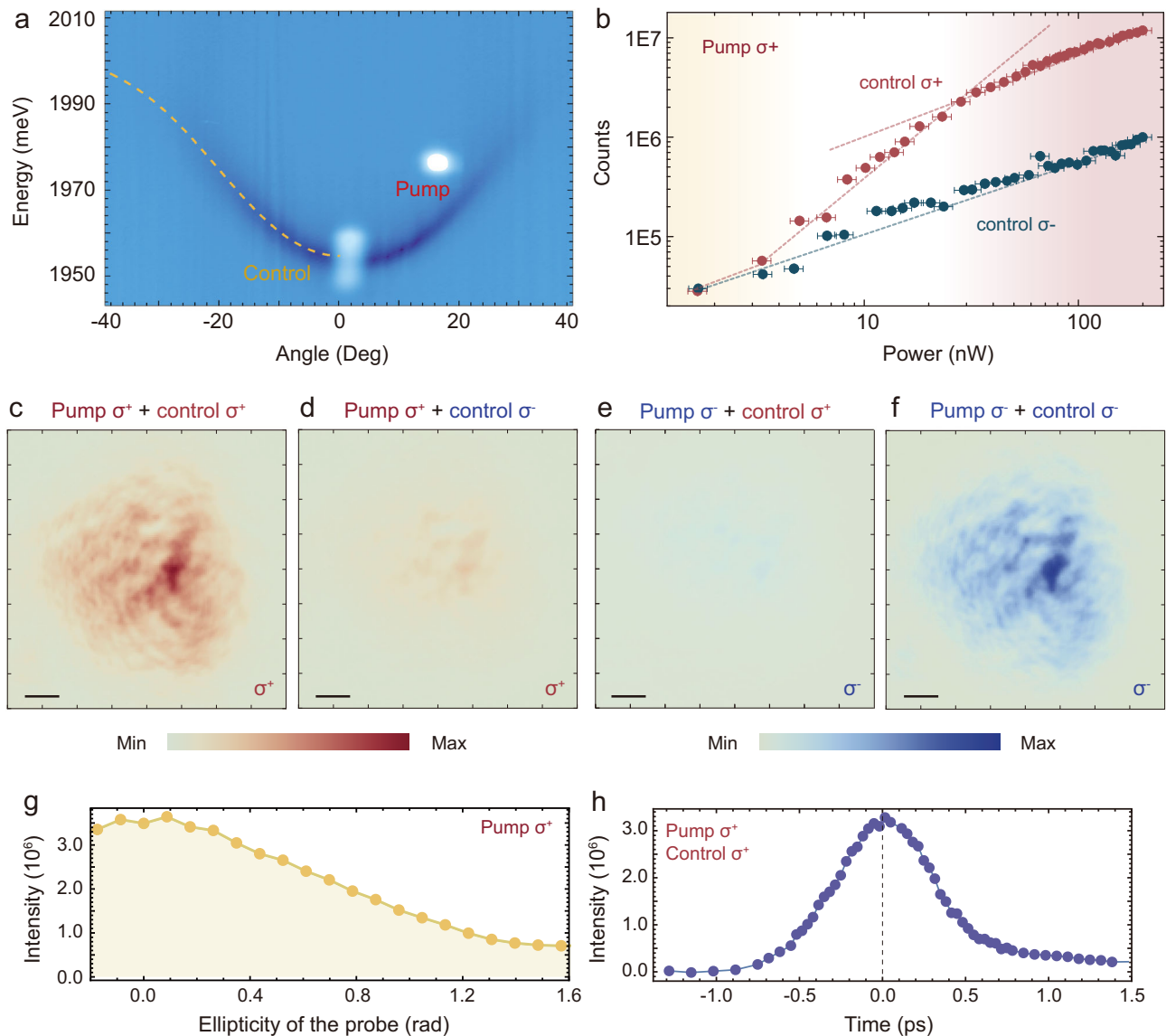
Fig. 3 | Spin switch based on the superlattice microcavity. a Schematic of the experimental configuration with two beams focused on the same spatial position with two different incident angles and energies. The yellow dashed curve indicates the LPB. **b** Integrated transmitted real space signal as a function of the control beam power and polarization, $\sigma+$ (red dots) and $\sigma-$ (blue dots), respectively. The threshold for the co-circularly polarized excitation scheme is clearly visible. The yellow and red regions indicate the OFF and ON state region, respectively. The top-left label indicates the polarization of the pump while the detection line is co-circular with the pump polarization. The reported counts are integrated over the whole spot size. **c–f** Results of the combined effect of co-circularly and cross-circularly polarized pump and control, respectively. When the control polarization is changed to the cross-circular polarization, no enhancement of transmission is observed. The bottom-right label indicates the polarization of the detection line. Scale bar is 1 μm. **g** Integrated transmitted intensity of the pump beam as a function of the ellipticity of the control beam. The point of maximum/minimum transmission indicates the co/cross-circular polarization state. The top-right label indicates the polarization of the pump while the detection line is co-circular with the pump polarization. **h** Transient transmission signal versus the time delay between the two beams.

spin-dependent Gross-Pitaevskii equations for polaritons, which quantitatively reproduce these experimental results under the same pulsed conditions. Our results clearly demonstrate the feasibility of polariton-based spintronic devices working at room temperature and are a fundamental step for future applications. These results not only mark a significant advancement in the field but also pave the way for the development of polaritonic devices embedding TMDs that harness spin-dependent interaction-driven phenomena.

Discussion

A roadmap on excitonic computing was published recently[46], explicitly identifying spintronic logic with excitons and exciton-polaritons as one of the most promising routes. We refer to this work for a survey of the

existing state-of-the-art and note that it also identifies the need for cryogenic cooling in existing proof-of-concept experiments[7] as the critical issue in exciton spintronics. This is precisely what we address in the present work. It is also important to note that recent reports have shown the potential of valley-polaritons for the implementation of polarization-sensitive devices[22–24]. Although a strong polarization response of the photoluminescence emission has been achieved, these works do not exploit the nonlinear regime, a fundamental requirement for the realization of polariton devices. Our work shows the practical development of devices that exploit polariton nonlinearities, a feature that underscores the unique appeal of polaritons. However, the application of TMD polaritons is currently constrained by the methodology employed, with the largest limitation being the restricted in-plane propagation observed
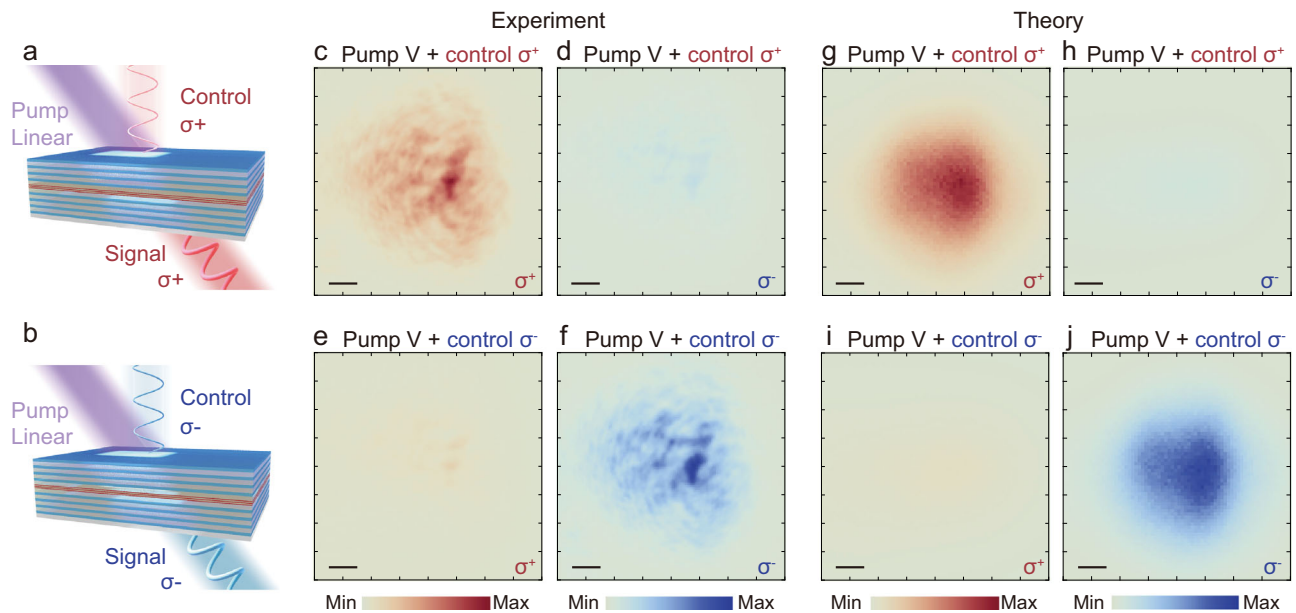
Fig. 4 | Spin switch in different polarizations. a, b Schematic of the experimental configuration of the spin switch with a linearly polarized pump and circularly polarized control. The transmitted pump signal (with linear polarization being a superposition of $\sigma-$ and $\sigma+$) is always co-polarized with the control beam. **c–f** Real-space experimental images of the transmitted pump signal. In the presence of a circularly polarized control beam either $\sigma+$ (c and d) or $\sigma-$ (e and f), the emission of the whole spot become co-polarized with the control beam. The bottom-right label indicates the polarization of the detection line. **g–j** Results from the numerical solution of the Gross- Pitaevskii equations, corresponding to the conditions of **c–f** respectively.

in state-of-the-art TMD microcavities. Indeed, any logic architecture needs to cascade, allowing for the sequential processing of signals from one stage to the next. This fundamental requirement cannot be satisfied without a suitable in-plane propagation, *i.e.* long polariton lifetime, and represents a concrete limitation of our samples. Additionally, the constrained spatial extension of the ML flakes, resulting from mechanical exfoliation, poses another significant challenge. In this respect, chemical vapor deposition (CVD) offers a scalable fabrication approach for depositing 2D materials over wafer-scale areas[30]. This advancement could significantly broaden the possibilities for designing TMD polaritons, offering new pathways to overcome the current limitations.

In this work, we present an investigation of polarization-dependent interactions between polaritons in WS$_2$-superlattice microcavities embedding up to three separated layers. Our results reveal that polaritons formed in multilayer structures exhibit extremely robust spin-dependent interactions at room temperature, a fundamental property to realize polariton-based spin devices. The presence of spin-dependent interactions has been exploited to demonstrate a proof-of-concept polariton spin switch where a weak control beam can effectively switch ON and actively modify the polarization of a pump beam. Unlike other previously proposed proof-of-concept devices operating at room temperature, our approach represents the first demonstration exploiting spin-dependent polariton nonlinearities for the realization of polariton devices effectively harnessing the spin degree of freedom of polaritons. It is important to note that the intrinsic short lifetime of the sample allows an ultrafast switching time that is two orders of magnitude faster than GaAs-based microcavities. Our results pave the way for novel applications for polariton-based spintronic devices. Further developments in this direction could also be achieved by using van der Waals heterostructure and wafer-scale growth methods to develop new on-chip integrated electronic devices.

Methods
Superlattice and microcavity fabrication
The WS$_2$ superlattice microcavity is composed of a $\lambda_{Exc}/2$ microcavity that is sandwiched between two DBR mirrors. The bottom DBR is composed of seven alternating pairs of titanium dioxide (TiO$_2$) and silicon dioxide (SiO$_2$) deposited by using electron-beam evaporation (Cello, Ohmiker-50B) onto a glass substrate. A transparent substrate is required to perform transmission measurements. Subsequently, the first $\lambda_{Exc}/4$-SiO$_2$ spacer was deposited onto the bottom DBR mirror using the same fabrication technique. A mixed-dimensional superlattice consisting of alternating layers of ML WS$_2$ and SiO$_2$ insulating layers with a thickness of ~4 nm was then assembled. The same electron-beam evaporator was used to deposit the thin SiO$_2$ layer. All the WS$_2$ MLs were mechanically exfoliated from the same bulk crystal, procured from HQ-Graphene with 2H phase. For details, the mechanically exfoliated ML was prepared using the scotch tape method and transferred onto a bottom DBR via a dry transfer technique with the aid of a polydimethylsiloxane (PDMS, PF-X4, Gel-Pack) stamp. Following this, a thin layer of SiO$_2$ was deposited via an E-beam evaporator. The second ML was then exfoliated onto a PDMS stamp. Using a home-built transfer stage, a top WS$_2$/PDMS film was meticulously aligned with the first ML and subsequently placed onto the surface. Upon removal of the PDMS layer, the second ML was aligned with the first ML and positioned on top of the SiO$_2$ layer. The superlattice (N3) structure was fabricated by repeating this process three times. A layer of poly (methyl methacrylate, PMMA) was spin-coated onto the bottom DBR containing the superlattice structure. Finally, as for the top mirror, a small piece of 6.5-pair DBR was transferred onto the PMMA layer, precisely positioned over the superlattice structure, using the same PDMS micro-transfer process. Further information regarding this transfer technique can be found in ref. 47.

Polariton nonlinearities and optical switching measurements
Two microscope objectives with large numerical apertures of 100× (NA = 0.9) and 50× (NA = 0.45), were used in reflection and transmission configuration, respectively. The dispersion presented in Fig. 1 was obtained by collecting white light in the reflection configuration. The polariton dispersion was resolved by imaging the back aperture of the microscopy objective (Fourier plane) onto the camera (see Supplementary Fig. S5). Specifically, the signal from the microcavity was collected through the narrow slit of a Horiba iHR550 spectrometer

equipped with three gratings (150 lines/mm, 600 lines/mm, 1800 lines/mm) and coupled to a 2D charge-coupled device array (Horiba, Symphony II), to achieve optimal spatial and spectral resolution.

To investigate spin-dependent interactions, a pulsed laser was employed in our experimental setup. The excitation pulsed source was derived from a Ti: sapphire laser that was equipped with an ultrafast amplifier (Spectra-Physics) and a computer-controlled Optical Parametric Amplifier for wavelength modulation. The repetition rate was 1 KHz, and the pulse width was -100 fs. The output beam was split into two paths, where one beam was directed through a mechanical delay line (Newport, M-ILS 150CC DC Servo Linear Stage) and served as the control beam to introduce the blueshift of the polariton mode. This beam excited the microcavity at $k = 0$ and was spectrally filtered using a band-pass filter. The precise energetic position of the filter was adjusted by controlling the tilt angle.

Referring to data concerning the spin-dependent interactions, we calculate the incident pulsed energy $E_{tot} = P/R$, where P denotes the excitation power and R = 1 kHz is the repetition rate of our pulsed laser. The excitation spot area was S - 20 μm^2, with a diameter of -5 μm. As displayed in Supplementary Fig. S5, the quarter-waveplate, half-waveplate, and linear polarized components were utilized to modify the polarization of the control beam. To estimate the polariton density, a conservative approximation was made, considering the total injected energy was completely absorbed. The energy absorbed by the LPB at $k = 0$ can be evaluated by calculating the integral of the absorption peak under the injected laser profile. The injected photon energy was estimated as follows:

$$E_{INJ} = \frac{E_{tot} \int A_{abs,LP}}{\int A_{laser,LP}} \qquad (1)$$

Herein, the $\int A_{abs,LP}$ represents the integral of the dip of the ground state, while $\int A_{laser,LP}$ denotes the integral of the laser profile. Specifically, for the dip of the dispersion, we have estimated the injected photon number, which can be related to the polariton density through the photonic fraction (C) of the ground state, according to the following relation: $n_{ph} = n_{pol}C$. By making the assumptions of laser injection, the polariton density can be estimated as $n_{pol} = \frac{n_{ph}}{C} = \frac{E_{inj}}{C A_{beam} E_{LP}}$, where E_{LP} is the energy of the ground state, and A_{beam} is the beam area, respectively. For a superlattice, we have calculated the polariton density per layer, thus dividing the overall polariton density by the total number of layers.

During the optical spin switch measurements, a second beam was employed, which was slightly off-resonance and served as the pump beam. A notch filter was utilized to spectrally filter this beam. The experimental results depicted in Fig. 3 were obtained by utilizing a circularly polarized pump and a circularly polarized control beam, whereas those presented in Fig. 4 were acquired by employing linearly polarized pump and circularly polarized control beams. The pump and control beams were focused on the microcavity with a beam size of -5 μm.

Theoretical calculations

With coherent pump injected, the dynamics of exciton-polaritons can be expressed by the Gross-Pitaevskii equation as:

$$i\hbar \frac{\partial \Psi_\pm}{\partial t} = \left(\hat{E}_{LP} - i\gamma + \alpha_1 |\Psi_\pm|^2 + \alpha_2 |\Psi_\mp|^2 \right) \Psi_\pm + F_\pm + P_\pm \qquad (2)$$

Here $\Psi_\pm$ is the wavefunction of polaritons in two-dimensional real space for which the $\pm$ symbols correspond to two circular polarizations. $\hat{E}_{LP}$ is the operator for the kinetic energy of polaritons in the lower polariton band, which can be written as:

$$\hat{E}_{LP}(k) = \frac{E_c(k) + E_x(k) - \sqrt{[E_c(k) - E_x(k)]^2 + \Omega^2}}{2} \qquad (3)$$

E_c, E_x are the energies for cavity photon and exciton modes, respectively, which are described by parabolic dispersion with effective masses m_c, m_x. Ω is the Rabi splitting, which equals to 66 meV in the simulation (the same as the experiment). γ is the polariton decay rate. α_1, α_2 are the strengths of polariton-polariton interactions between parallel and antiparallel spins. In our theoretical model, we consider two coherent laser pulses corresponding to pump, $F_\pm$, and control, $P_\pm$:

$$F_\pm = F_{0,\pm} e^{ik_p x} e^{-i\omega t} e^{-\frac{(x-x_0)^2}{dx^2}} e^{-\frac{(y-y_0)^2}{dy^2}} e^{-\frac{(t-t_0)^2}{dt^2}} \qquad (4)$$

$$P_\pm = P_{0,\pm} e^{-i\omega_o t} e^{-\frac{(x-x_0)^2}{dx^2}} e^{-\frac{(y-y_0)^2}{dy^2}} e^{-\frac{(t-t_0)^2}{dt^2}} \qquad (5)$$

$F_{0,\pm}, P_{0,\pm}$ are the amplitudes of the coherent laser pulses; k_p is the pump in-plane wavevector; ω is the angular frequency of the pulse, (x_0, y_0) is the center position of the pulses; dx, dy are the widths of the pulses and dt is the pulse duration. For parameters in the simulation, we take $m_c = 2 \times 10^{-5} m_e$ (m_e is the free electron mass), $\gamma = 0.6 meV$, $\alpha_1 = 0.1 ueV\ um^2, \alpha_2 = -0.1\alpha_1$ which are taken in agreement with experimental values. For the pulse's parameters, we take directly from our experimental values.

Data availability

All data needed to evaluate the conclusions in the paper are present in the paper and/or the Supplementary Materials. Additional data related to this paper may be requested from the authors.

References

1. Žutić, I., Fabian, J. & Das Sarma, S. Spintronics: fundamentals and applications. *Rev. Mod. Phys.* **76**, 323–410 (2004).
2. Soumyanarayanan, A., Reyren, N., Fert, A. & Panagopoulos, C. Emergent phenomena induced by spin–orbit coupling at surfaces and interfaces. *Nature* **539**, 509–517 (2016).
3. O'Brien, J. L., Furusawa, A. & Vučković, J. Photonic quantum technologies. *Nat. Photonics* **3**, 687–695 (2009).
4. Wang, J., Sciarrino, F., Laing, A. & Thompson, M. G. Integrated photonic quantum technologies. *Nat. Photonics* **14**, 273–284 (2020).
5. Nishikawa, Y., Tackeuchi, A., Yamaguchi, M., Muto, S. & Wada, O. Ultrafast all-optical spin polarization switch using quantum-well etalon. *IEEE J. Sel. Top. Quantum Electron.* **2**, 661–667 (1996).
6. Pearton, S. J. et al. Advances in wide bandgap materials for semiconductor spintronics. *Mater. Sci. Eng.: R: Rep.* **40**, 137–168 (2003).
7. Amo, A. et al. Exciton–polariton spin switches. *Nat. Photonics* **4**, 361 (2010).
8. Sanvitto, D. & Kéna-Cohen, S. The road towards polaritonic devices. *Nat. Mater.* **15**, 1061–1073 (2016).
9. Amo, A. et al. Superfluidity of polaritons in semiconductor microcavities. *Nat. Phys.* **5**, 805–810 (2009).
10. Deng, H., Haug, H. & Yamamoto, Y. Exciton-polariton bose-einstein condensation. *Rev. Mod. Phys.* **82**, 1489 (2010).
11. Adrados, C. et al. Motion of Spin Polariton Bullets in Semiconductor Microcavities. *Phys. Rev. Lett.* **107**, 146402 (2011).
12. Zasedatelev, A. V. et al. A room-temperature organic polariton transistor. *Nat. Photonics* **13**, 378–383 (2019).
13. Feng, J. et al. All-optical switching based on interacting exciton polaritons in self-assembled perovskite microwires. *Sci. Adv.* **7**, eabj6627 (2021).

14. Chen, F. et al. Optically controlled femtosecond polariton switch at room temperature. *Phys. Rev. Lett.* **129**, 057402 (2022).

15. Vladimirova, M. et al. Polariton-polariton interaction constants in microcavities. *Phys. Rev. B* **82**, 075301 (2010).

16. Kammann, E. et al. Nonlinear optical spin hall effect and long-range spin transport in polariton lasers. *Phys. Rev. Lett.* **109**, 036404 (2012).

17. Dreismann, A. et al. A sub-femtojoule electrical spin-switch based on optically trapped polariton condensates. *Nat. Mater.* **15**, 1074–1078 (2016).

18. Paraïso, T. K., Wouters, M., Léger, Y., Morier-Genoud, F. & Deveaud-Plédran, B. Multistability of a coherent spin ensemble in a semiconductor microcavity. *Nat. Mater.* **9**, 655–60 (2010).

19. Ghosh, S. et al. Microcavity exciton polaritons at room temperature. *Photonics Insights* **1**, R04 (2022).

20. Wang, Q. H., Kalantar Zadeh, K., Kis, A., Coleman, J. N. & Strano, M. S. Electronics and optoelectronics of two-dimensional transition metal dichalcogenides. *Nat. Nanotechnol.* **7**, 699 (2012).

21. Zeng, H., Dai, J., Yao, W., Xiao, D. & Cui, X. Valley polarization in MoS_2 monolayers by optical pumping. *Nat. Nanotechnol.* **7**, 490–493 (2012).

22. Sun, Z. et al. Optical control of room-temperature valley polaritons. *Nat. Photonics* **11**, 491 (2017).

23. Dufferwiel, S. et al. Valley-addressable polaritons in atomically thin semiconductors. *Nat. Photonics* **11**, 497 (2017).

24. Chen, Y.-J., Cain, J. D., Stanev, T. K., Dravid, V. P. & Stern, N. P. Valley-polarized exciton–polaritons in a monolayer semiconductor. *Nat. Photonics* **11**, 431 (2017).

25. Lundt, N. et al. Optical valley Hall effect for highly valley-coherent exciton-polaritons in an atomically thin semiconductor. *Nat. Nanotechnol.* **14**, 770–775 (2019).

26. LaMountain, T. et al. Valley-selective optical Stark effect of exciton-polaritons in a monolayer semiconductor. *Nat. Commun.* **12**, 4530 (2021).

27. Zhao, J. et al. Nonlinear polariton parametric emission in an atomically thin semiconductor based microcavity. *Nat. Nanotechnol.* **17**, 396–402 (2022).

28. Dufferwiel, S. et al. Valley coherent exciton-polaritons in a monolayer semiconductor. *Nat. Commun.* **9**, 4797 (2018).

29. Dufferwiel, S. et al. Exciton–polaritons in van der Waals heterostructures embedded in tunable microcavities. *Nat. Commun.* **6**, 8579 (2015).

30. Kumar, P. et al. Light–matter coupling in large-area van der Waals superlattices. *Nat. Nanotechnol.* **17**, 182–189 (2022).

31. Zhao, J. et al. Exciton polariton interactions in Van der Waals superlattices at room temperature. *Nat. Commun.* **14**, 1512 (2023).

32. Hu, Z. et al. Energy transfer driven brightening of MoS_2 by ultrafast polariton relaxation in microcavity MoS_2/hBN/WS_2 heterostructures. *Nat. Commun.* **15**, 1747 (2024).

33. Ballarini, D. et al. Transition from the strong-to the weak-coupling regime in semiconductor microcavities: polarization dependence. *Applied physics letters* **90**, 201905 (2007).

34. Fieramosca, A. et al. Two-dimensional hybrid perovskites sustaining strong polariton interactions at room temperature. *Sci. Adv.* **5**, eaav9967 (2019).

35. Liu, T. Y. et al. Dynamics of spin-dependent polariton–polariton interactions in two-dimensional layered halide organic perovskite microcavities. *Laser Photonics Rev.* **16**, 2200176 (2022).

36. Fieramosca, A. et al. Origin of exciton–polariton interactions and decoupled dark states dynamics in 2D hybrid perovskite quantum wells. *Nano Lett.* **24**, 8240–8247 (2024).

37. Shelykh, I. A., Kavokin, A. V., Rubo, Y. G., Liew, T. & Malpuech, G. Polariton polarization-sensitive phenomena in planar semiconductor microcavities. *Semiconductor Sci. Technol.* **25**, 013001 (2009).

38. Sun, K., Shen, K., Gelin, M. F. & Zhao, Y. Exciton dynamics and time-resolved fluorescence in nanocavity-integrated monolayers of transition-metal dichalcogenides. *J. Phys. Chem. Lett.* **14**, 221–229 (2022).

39. Choo, K., Bleu, O., Levinsen, J. & Parish, M. M. Polaronic polariton quasiparticles in a dark excitonic medium. *Phys. Rev. B* **109**, 195432 (2024).

40. Emmanuele, R. et al. Highly nonlinear trion-polaritons in a monolayer semiconductor. *Nat. Commun.* **11**, 3589 (2020).

41. Song, K. W., Chiavazzo, S., Shelykh, I. A. & Kyriienko, O. Theory for coulomb scattering of trions in 2D materials. *arXiv preprint arXiv:2207.02660* (2022).

42. Stepanov, P. et al. Exciton-exciton interaction beyond the hydrogenic picture in a $MoSe_2$ monolayer in the strong light-matter coupling regime. *Phys. Rev. Lett.* **126**, 167401 (2021).

43. Barachati, F. et al. Interacting polariton fluids in a monolayer of tungsten disulfide. *Nat. Nanotechnol.* **13**, 906 (2018).

44. Liu, B. et al. Long-range propagation of exciton-polaritons in large-area 2D semiconductor monolayers. *ACS Nano* **17**, 14442–14448 (2023).

45. Maggiolini, E. et al. Strongly enhanced light–matter coupling of monolayer WS_2 from a bound state in the continuum. *Nat. Mater.* **22**, 964–969 (2023).

46. Hudson, R. J. et al. A framework for multiexcitonic logic. *Nat. Rev. Chem.* **2**, 136–151 (2024).

47. Rupprecht, C. et al. Micro-mechanical assembly and characterization of high-quality Fabry–Pérot microcavities for the integration of two-dimensional materials. *Appl. Phys. Lett.* **118**, 103103 (2021).

Acknowledgements

Author contributions

A.F., J.Z., and T.L. conceived the ideas and designed the experiments. J.Z. prepared superlattice microcavity samples. J.Z. and A.F. carried out the optical spectroscopy measurements and analyzed data. R.B. and K.D. performed theoretical calculations. J.Z., A.F., R.S., D.S. Q.X., and T.L. wrote the manuscript with contributions from all authors. All authors discussed the results and commented on the manuscript.

Competing interests

The authors declare no competing interests.

Additional information

Supplementary information The online version contains supplementary material available at https://doi.org/10.1038/s41467-024-51612-2.

Correspondence and requests for materials should be addressed to Antonio Fieramosca, Qihua Xiong or Timothy C. H. Liew.

Peer review information *Nature Communications* thanks the anonymous reviewers for their contribution to the peer review of this work. A peer review file is available.

Reprints and permissions information is available at http://www.nature.com/reprints

Publisher's note Springer Nature remains neutral with regard to jurisdictional claims in published maps and institutional affiliations.